Resonant Geometries for Circulation Pattern Macroinstabilities in a Stirred Tank

V. T. Roussinova and S. M. Kresta
Dept. of Chemical and Materials Engineering, University of Alberta, Edmonton, Alberta T6G 2N8, Canada

R. Weetman
Lightnin, Rochester, NY 14611

DOI 10.1002/aic.10275

Circulation pattern macroinstabilities and precessing vortices are known to exist in stirred tanks, but until recently they have eluded a full quantitative analysis. In this article, frequency analysis of the axial velocity reveals a resonant frequency and geometry for the 45° pitched-blade turbine (PBT) in a flat-bottom cylindrical tank. Unlike other axial impellers, such as the hydrofoils A310 and HE3, the PBT produces a large-scale circulation macroinstability at the scale of the vessel diameter. The macroinstability is superimposed on the turbulent random fluctuations with a timescale that is very long compared to the blade passage frequency and the inertial convective range of the turbulent cascade. In this article it is shown that the circulation pattern macroinstabilities generated by the 45° PBT are coherent and propagate throughout the tank only under very specific conditions ($D = T/2$ and $C/D = 0.50$). The normalized frequency of the coherent macroinstability, or Strouhal number, is $f_{MI}/N = 0.186$. This corresponds to a period of roughly five rotations of the impeller, or 20 individual blade passages. The laser Doppler velocimeter data used in this work are unevenly spaced because they are collected in burst detection mode. This severely complicates spectral or frequency analysis. Standard algorithms such as the fast Fourier transform, autocorrelation methods, and wavelet analysis all require evenly spaced data. The Lomb periodogram was successfully used to extract the low-frequency content of the unevenly spaced data with a higher accuracy than is possible with other methods. The Lomb method also eliminates a short time-averaging step that was required in earlier work. © 2004 American Institute of Chemical Engineers *AIChE J,* 50: 2986–3005, 2004

Introduction

In the cylindrical stirred tank used throughout the chemical process industries, macroinstabilites in the gross circulation pattern can cause strong vibrations, unsteady loading, and even mechanical damage to tank internals. The vibrations are a significant problem in plant operations. When these vibrations are large, tanks may have to be shut down until the problem can be resolved.

Three ranges of frequencies are present in the tank and different flows are associated with each frequency range. First, at any instant the velocity field contains a whole spectrum of high frequencies arising from turbulent eddies and vortices. Second, there are trailing vortices close to the tip of the impeller blades. If the blade width is $D/5$, where D is the impeller diameter, then the trailing vortices are approximately $D/10$ in diameter. These trailing vortices are present only in the region surrounding the impeller. They do not extend out to the

---

R. Weetman is currently at rjweetman.com (e-mail: ron@rjweetman.com).
Correspondence concerning this article should be addressed to S. M. Kresta at suzanne.kresta@ualberta.ca.

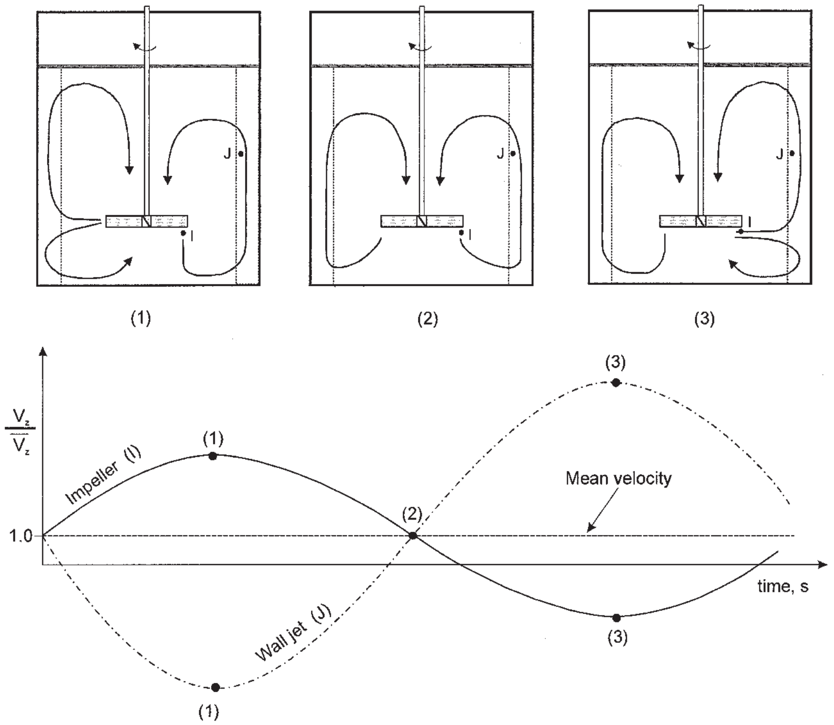

Figure 1. Illustration of the different circulation patterns which make up the macroinstability (MI) (45° PBT, $C/D = 0.5$, and $D = T/2$, $10^4 < \mathrm{Re} \leq 10^5$).

As the circulation pattern changes, the macroinstability is recorded as a low-frequency variation in the axial velocity. The phase and amplitude of the signal vary throughout the tank, but the frequency does not (not to scale).

tank walls. Finally, macroinstabilites are present, throughout the tank, with a length scale of the order of the tank diameter. These macroinstabilites may be precessing vortices revolving about the shaft or slow changes in the whole circulation pattern.

Figure 1 illustrates the effect of a circulation pattern macroinstability on the axial velocity. At the top, three phases of the changing circulation pattern produced by a 45° pitched-blade turbine (PBT) are illustrated. This variation in the circulation pattern is the macroinstability of interest. Figure 1 (bottom) shows the effect of the macroinstability on the axial velocity at two probe locations: the first in the impeller stream (I) and the second in the wall jet (J). As the impeller discharge stream at I oscillates between the bottom of the tank [Figure 1(1)] and the side wall [Figure 1(3)], a low-frequency, high-amplitude variation in the velocity is observed at both I and J. The frequency is the same at both positions I and J. When a laser Doppler velocimeter (LDV) is used to probe the flow at these locations, the smoothed axial velocity records show similar low-frequency, high-amplitude oscillations. The measured velocity time series are more complicated because of the presence of turbulent fluctuations and fluctuations associated with blade passages close to the impeller. As the probe is moved away from the impeller the blade passage frequency (BPF) quickly dies away. The macroinstability arising from changes in the circulation pattern (Figure 1) is superimposed on the turbulent random fluctuations with a timescale that is very long compared to the characteristic BPF and turbulent cascade and persists after the BPF dies away.

Before proceeding with the current macroinstability analysis, previous papers on macroinstabilities are briefly reviewed. The reader will note that the observations of macroinstability are sensitive to both tank geometry and measurement location. An attempt is made, a posteriori, to explain the existing observations and to place them in a larger context.

Winardi et al. (1988) were among the first to report macroinstabilities. Using flow visualization, they found that the instantaneous flow field close to a paddle impeller (four-bladed 90° paddle impeller, $T = 0.40$ m, $D = 0.16$ m, $C = 0.20$ m) is different from the mean velocity field as measured using LDV. Quite different flow patterns and various combinations of patterns appear over time. This work suggested a shift in the analysis of the stirred tank flow fields: a single circulation pattern might not represent conditions in the vessel, any more than the average of a sinusoidal function is representative of a sine wave.

Kresta and Wood (1993a,b) also observed circulation pattern macroinstabilites when they probed the flow field of a 45° PBT impeller ($T = 0.152$ m, $D = T/2$ and $T/3$, various clearances) using flow visualization, LDV, and spectral analysis. They demonstrated that there is a change in the stable circulation pattern as the off-bottom clearance of the impeller is changed. They reported low-frequency variations in the velocity signal that they were not able to explain. The low frequencies were not always present. A later paper by Chapple and Kresta (1994) considered the effect of off-bottom clearance, impeller diameter, and number of baffles on mean flow stability for two axial impellers: the Lightnin fluidfoil A310 impeller and the PBT. They found that the impeller geometry is the most important variable when the tank is fully baffled: the flow for the A310 was consistently much more stable than that for the PBT. For the A310 a single mean circulation pattern was, in fact, representative. Roussinova et al. (2000) followed up on this work, using a smoothed velocity signal to show that the macroinstability is dominant for the 45° PBT impeller but is much less important for hydrofoil impellers (HE3 and A310), and for the Rushton turbine (RT). For the RT, trailing vortices dominate the velocity signal close to the impeller. These differences between impellers are extremely important for mechanical design specifications.

Bruha et al. (1993) investigated three-, four-, and six-bladed PBTs, showing no clear effect of blade number on the results. They also studied the effect of impeller rotational speed and the different geometries in which macroinstabilities occur. Their investigations covered two small impeller diameters ($D = T/3$ and $T/4$), and three different off-bottom clearances ($T = 0.3$ m, $C/T = 0.33$, 0.4, and 0.5). They observed a vortex that appears as a welling up of the fluid surface close to the baffle and that scales linearly with the impeller rotational speed. Later work from this group (Bruha et al., 1994, 1995, 1996) uses flow visualization and a "tornadometer." The tornadometer target is placed below the surface in the vicinity of the impeller. The target is deflected whenever the circulation pattern macroinstabilities are strong enough to change the direction of the mean flow from axial to radial. Once again the macroinstabilities scale linearly with the impeller rotational speed and the low-frequency macroinstabilities are associated with changes in the circulation pattern, although the macroinstability measured with the tornadometer is not necessarily the same as that observed in the surface welling experiments.

Montes et al. (1997) used LDV measurements, flow visualization, spectral analysis, and wavelets to analyze the flow in a stirred tank equipped with a small six-bladed 45° PBT impeller ($T = 0.30$ m, $D = T/3$, $C/T = 0.35$, four baffles). They suggest that the occurrence of macroinstabilities is accompanied by the presence of a large precessing vortex in the upper part of the vessel, and that the vortex precession is linearly coupled with the frequency of the impeller revolution. They observed the precessing vortex macroinstability in both the transitional ($600 < \mathrm{Re} < 20{,}000$) and fully turbulent ($\mathrm{Re} > 20{,}000$) flow regimes. Hasal et al. (2000) studied the same geometry, using proper orthogonal decomposition (POD) to calculate the correlation dimension and the largest Lyaponov exponent λ_{max}. They found no coherent frequency close to the impeller at turbulent Reynolds numbers. Note that for both of these studies, a small $D = T/3$ impeller was used. The results of the present work will show that for a smaller impeller diameter, the circulation pattern macroinstability is not coherent, so the precessing vortex might be expected to dominate for this configuration.

Myers et al. (1997) used digital particle image velocimetry (DPIV) to characterize macroinstabilities in the flow field driven by a small four-bladed 45° PBT ($T = 0.145$ m, $D = 0.35T$, $C = 0.33T$ and $0.46T$). They analyzed spatially averaged vorticity from DPIV velocity time series covering 40 to 300 impeller revolutions. The authors found that the trailing vortices arising from the blade passages did not influence the macroinstabilities in the circulation pattern.

Nikiforaki et al. (2003) focused on the region close to the shaft in the upper portion of the tank. The frequency they observed matches a forced vortex driven by the rotating shaft, as shown by Kresta and Roussinova (2004). This suggests that a precessing vortex is convected around the shaft by the angular velocity field in the top part of the vessel. One might ask whether the precessing vortex is truly an instability in the flow, or is more accurately described as a large coherent structure convected by the mean flow. Regardless of the underlying physics, the very low frequency of the vortex precession is also significant for mechanical design of large vessels.

The presence of long timescale, high-amplitude variations in the flow field also has significant implications for the accurate measurement and simulation of small-scale turbulence in stirred tanks. This was first pointed out by Kresta and Wood (1993b), and has since been discussed in more detail by both Kresta (1998), who showed the effect of amplitude on the error for a model signal, and by Roussinova et al. (2000), who examined circulation pattern macroinstabilities for a range of tank and impeller geometries, particularly with respect to the associated errors in root mean square (RMS) velocity measurement.

This report progresses from documenting the evidence of macroinstabilities at a single location in the tank to quantifying their frequency and how it propagates throughout the vessel. This allows us to isolate resonant geometries and separate circulation pattern macroinstabilities from precessing vortices. All macroinstabilities are large-scale fluctuations with a period much longer than the blade passages: to measure their frequency, many low-period oscillations must be acquired in a single time series. The frequency analysis of these long, unevenly spaced time series requires a spectral estimator more advanced than the standard fast Fourier transform (FFT), and more efficient than the discrete Fourier transform (DFT).

Previous work by the authors (Roussinova et al., 2000) used velocity smoothing to analyze the low-frequency portion of the signal. This method requires selection of the size of the smoothing window for each velocity record. This is a reasonable undertaking for a small portion of the tank where the flow is relatively homogeneous, the data rates are high, and the frequency can be estimated a priori. In this work, however, a large fraction of the tank volume is examined. Mean velocity and data rates vary by up to a factor of 100 and the frequencies are not always known a priori. A method is needed to objectively isolate the low frequencies in the velocity signal, giving greater precision in the frequency extracted with no requirement to estimate the best smoothing window.

Three frequency analysis techniques are examined. Using simulated data, their performance is compared, with emphasis on accurate detection of the low frequency. The Lomb periodogram gives the best performance and it is used to analyze the flow driven by three axial impellers (45° PBT, A310, and HE3) at varying off-bottom clearances and Reynolds numbers. Resonant geometric conditions are identified where the circulation pattern macroinstabilities become coherent (resonant), meaning that they have a single frequency throughout the tank. This work relieves much of the ambiguity in the literature by expanding the scope of the investigation to a large area in the tank. This allows a clear discrimination between the circulation pattern macroinstability and other macroinstabilities. The results clearly identify resonant geometries where circulation pattern macroinstabilities dominate, and other geometries where the flow pattern is stable or where a combination of several different macroinstabilities is present.

2a) LDV signal

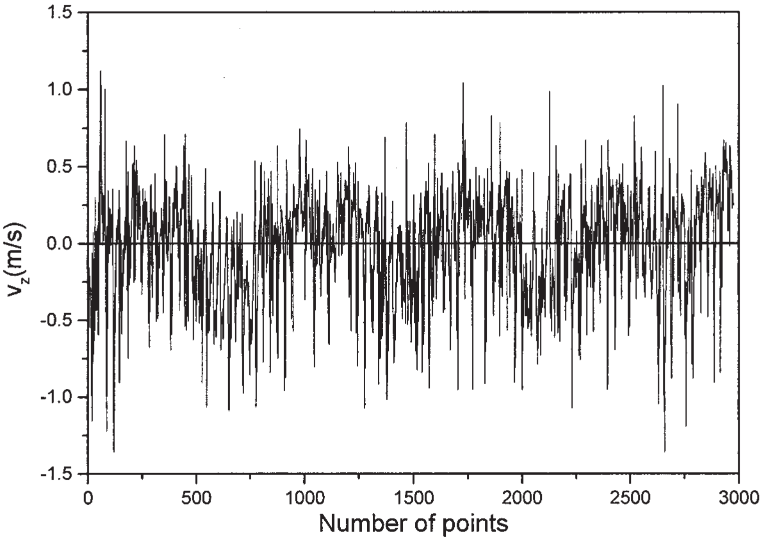

2b) FFT spectrum

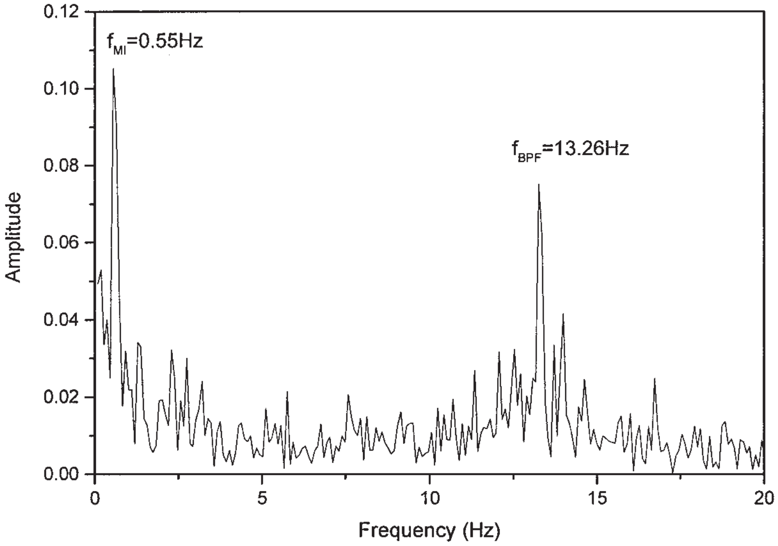

Figure 2. Comparison of frequency analysis results showing that the Lomb analysis returns the most defined frequency peak: (a) a representative mean-centered LDV signal, (b) its FFT, (c) its local wavelet power spectrum using the complex Morlet wavelet, and (d) Lomb frequency spectrum.

Frequency Analysis of Unevenly Spaced Data

A typical time series of the axial velocity measured in the impeller stream for the 45° PBT is shown in Figure 2a. The velocity record shows the turbulent fluctuations, the fluctuations arising from the individual blade passages at the impeller, and the fluctuations resulting from macroinstabilities. The high-intensity turbulent fluctuations tend to obscure the longer timescale fluctuations, whereas all of the information about the different length and velocity scales present in the flow is lost when only the mean velocity is considered. One way of distinguishing the macroinstabilities is to transform the velocity signal into the frequency domain where dominant periodic or quasi-periodic motions appear as peaks in the frequency spectrum. The transformation from the time domain to the frequency domain can be done using the standard FFT if the input signal is evenly spaced in time. This is not the case for the

2c) Local wavelet power spectrum

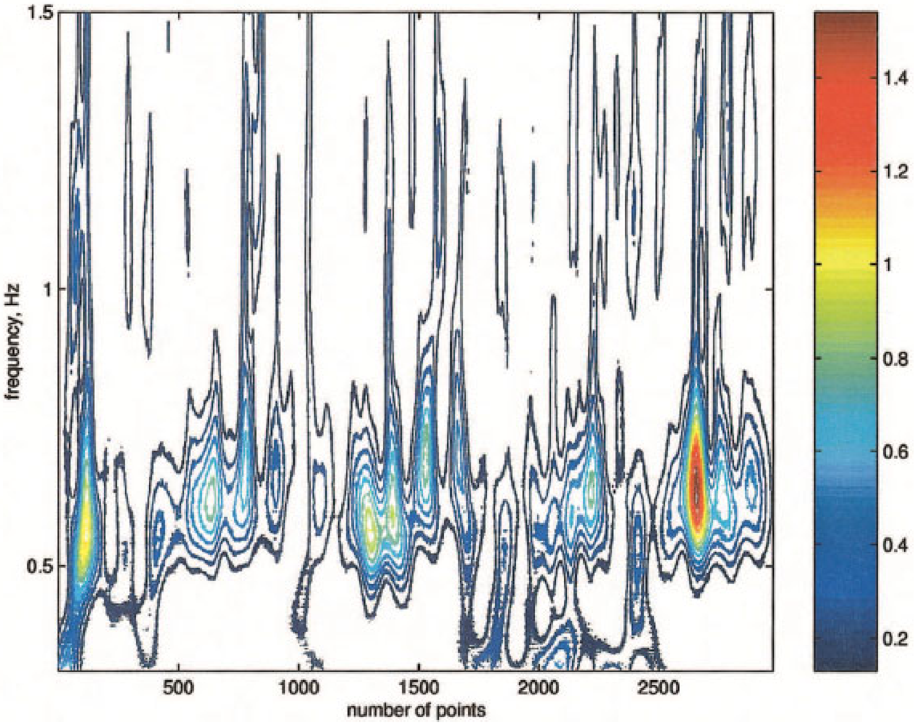

2d) Lomb frequency spectrum

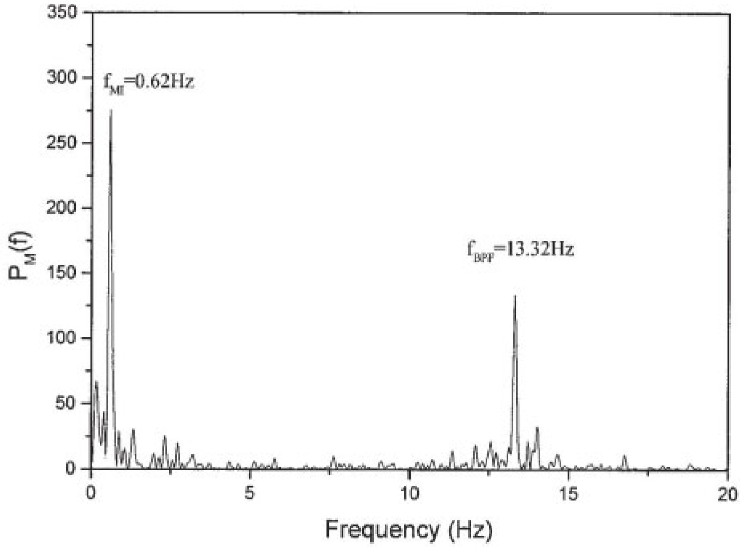

Figure 2 (continued)

velocity signals measured with burst-detection LDV. In burst-detection LDV mode, velocity measurements are taken as particles cross the measuring volume, meaning that the time between the samples follows a random, or Poisson, distribution. This makes frequency analysis more difficult. As partial compensation for the difficulty of analyzing unevenly spaced data, we note that there is no upper theoretical limit on the frequency range detectable from an unevenly sampled signal. This is in contrast to periodic sampling schemes where the highest frequency that can be calculated, the Nyquist frequency, is exactly half the sampling frequency: $f_N = 1/2\Delta$.

Numerous techniques for recovering power spectra from LDV data have been presented in the literature. Most of the improvements in these methods over the last decade concern retrieval of the true power spectral density, with emphasis on the high frequencies and spectral slopes (Benedict et al., 2000; Muller et al., 1998; van Maanen, 1999). However, the main interest in the present study does not concern the PSD and retrieval of the high-frequency turbulence properties. We seek a method that can operate directly on randomly sampled data and provide an exact and objective calculation of the dominant low frequency in the velocity signal. Existing frequency analysis methods are briefly reviewed and compared to select the best route for analysis of macroinstabilities.

Fast Fourier transform and discrete Fourier transform

The FFT algorithm is the fastest and most widely used spectral estimator. It is able to calculate the frequency content correctly only if the input data are equally spaced. Direct application of the fast Fourier transform to unevenly spaced data results in smeared-out and inaccurate frequency spectra and this method is mentioned here only by way of introduction to more appropriate methods. If one uses interpolation to model the unevenly sampled data as an equally spaced sequence, a complex frequency spectrum is likely to be distorted (Antonia and Britz, 1996). All interpolation procedures are computationally intensive and their implications are not clearly defined because of the complex nature of the turbulent signal.

DFT analysis of a set of unevenly spaced data is far more complex than DFT analysis of a uniform set of data, mostly because there is no frequency range in which a period is unambiguously defined (Scargle, 1982). The DFT is very computationally intensive.

Autocorrelation methods

A second way of extracting the overall signal characteristics from randomly sampled LDV data is to calculate the (auto)-power spectrum from a binned autocorrelation function. Gaster and Roberts (1975, 1977) provide a numerical procedure for these calculations. The major advantage of this method is that, because the autocorrelation products are collected in the equally spaced bins, the autocorrelation can be transformed to the frequency spectrum. The selected bin size, however, determines the accuracy of the low-frequency results. The size of the data record required to obtain an accurate spectrum expands as the number of bins increases.

A short time mean variation on the slotted autocorrelation technique was applied by Grgic (1998). The raw data record was processed by moving a fixed time window through it. All data points that fall into the window are averaged. The resulting evenly spaced data record is in effect low-pass filtered at a cutoff frequency approximately corresponding to the window size. This is similar to the "slotting" technique of Mayo et al. (1974). Its main drawback is that an appropriate window size must be determined. For best results, the window size must be selected for each time series: it cannot be unambiguously defined. A more robust and less labor intensive approach is needed.

Wavelet analysis

Wavelet analysis is useful for analyzing localized variations of power within a time series. By decomposing a time series into time–frequency space, one is able to determine both the dominant modes of variability and how those modes vary in time. This feature of wavelet analysis has been used as a tool for detecting coherent structures in turbulent flow, for study of intermittency, singularities, and fractal structure (Farge, 1992).

Among the various wavelet forms, consideration is given here to the complex-valued Morlet wavelet, defined as

$$\psi(x) = \exp(ik_0x)\exp\left(-\frac{1}{2}|x|^2\right) \tag{1}$$

where $k_0 = 6$ to make the wavelet admissible. This wavelet is a plane wave modulated by a Gaussian envelope of unit width. The Morlet wavelet was selected because the resulting averaged wavelet energy spectrum is very close to the Fourier energy spectrum, allowing direct comparison with FFT results (Bonnet et al., 1998).

The wavelet transform can be considered a complementary tool to FFT for analysis of turbulent signals. It can provide information about the scales, or coherent structures, present in the signal at each instant in time. This makes it attractive for further investigation; however, the wavelet method in its present form suffers from two disadvantages. First, the time series of interest have to be equally spaced, the same limitation as previously discussed for FFT. Second, although the wavelet transform provides much more detailed local information about the signal than the FFT, there is no clear theoretical basis for recognizing the dominant single frequency or structure in the local data.

Lomb periodogram

It was stated earlier that it is complicated to apply classical periodogram analysis (DFT) to unevenly sampled data in a rigorous way. Lomb (1976) derived a generalization of the classical periodogram for unevenly sampled data, based on the method of least squares. This method, known as the *Lomb method*, was shown by Scargale (1982) to be invariant with respect to time translation and to provide a statistical significance test for a perceived periodic signal.

The Lomb method is widely used for the analysis of astronomical signals, but is less familiar to the chemical engineering community. In the Appendix, a short derivation of the method is given. It has been modified from standard references (Lomb, 1976; Scargle, 1982) to clarify the key features of the method, while preserving mathematical rigor in the derivation. The Lomb algorithm is functionally and mathematically equivalent to the direct application of the discrete Fourier transform. Because it operates directly on unevenly spaced data it is a more precise method than FFT or wavelet analysis, both of which require some pretreatment of the signal to obtain evenly spaced data.

The Lomb analysis was selected for detection of the frequency of the macroinstabilitiy for several reasons. The first advantage of the Lomb method is its ability to operate directly on unevenly sampled data. The second is its ability to detect a periodic signal in noisy data. In LDV time series for a stirred tank, the macroinstability is obscured by the presence of the BPF and turbulence. Although these are real frequencies rather than measurement error, the effect is analogous to "noise" in the signal. The third advantage is the precision of the Lomb method in determining the single or multiple frequencies that may be known (BPF) or unknown (macroinstability) a priori. Like the binned autocorrelation method (Gaster and Roberts, 1977) the Lomb periodogram uses exact time information;

however, the Lomb method provides narrow peaks that allow a more accurate identification of the frequency of the macroinstability.

Numerical comparison of frequency analysis methods

To illustrate the implementation of the FFT, wavelet analysis, and Lomb analysis, a representative data record was selected, as shown in Figure 2a. The LDV data were collected just below the impeller tip at a high data rate, and contain all of the frequencies expected in the flow. Application of the FFT and wavelet algorithms precludes the use of unevenly sampled data, and thus the raw LDV signal was resampled using a sample-and-hold algorithm at a sampling frequency equal to half the average sampling frequency. This is possible because of the high data rate for this measurement location, although the sample-and-hold approach always introduces some error into the analysis. It is equivalent to a zero-order interpolation. The resampled signal has 3000 points at a sampling interval of $\Delta = 0.0025$ s.

Figure 2b shows the resulting FFT spectrum, with a broad peak centered at a frequency of $f = 0.55$ Hz. The Morlet wavelet analysis was applied to the same resampled data record and the resulting contour plot of the local wavelet power is shown in Figure 2c. The frequency scale was obtained by converting the wavelet spectrum to the frequency spectrum using a passband center of the Fourier transform as the representative frequency (Farge, 1992), as follows

$$f = \frac{k_0 + \sqrt{2 + k_0}}{4\pi s} \tag{2}$$

Most of the wavelet power is concentrated in the frequency band of 0.55–0.65 Hz. Finally, the Lomb method results are shown in Figure 2d. In the Lomb spectrum the frequency is precisely located at $f = 0.62$ Hz. Clearly, the Lomb method gives the best results for precise detection of the macroinstability frequency in this experimental signal.

A more rigorous test of the performance of the FFT and the Lomb algorithms relative to the exact DFT calculation was performed using a simulated signal whose spectral characteristics are similar to the experimental conditions. The test function has a signal with three frequency components 0.05, 0.62, and 16.67 Hz, with corresponding amplitudes of 1.0, 0.7, and 0.3

$$y(t) = 1.0\sin(2\pi 0.05t) + 0.7\cos(2\pi 0.62t) + 0.3\sin(2\pi 16.67t) \tag{3}$$

The number of macroinstability cycles in the data, or the total record length, was selected to cover different fractions of cycles: collection of an integer number of cycles in the data record will always minimize the error, but will occur only by chance in a real data set. For the FFT analysis, the function was sampled in two different ways. The first set of data was collected at different sampling rates, always giving a total of 4096 (2^{12}) evenly spaced points but over varying numbers of macroinstability cycles. For the second set of data, the sampling rate was fixed at 20.75 Hz and the length of the data record was extended to cover additional cycles of macroinstability. For the Lomb and DFT analysis, the function was unevenly sampled using a random time sequence, $t_m = m\Delta + r\Delta$, where Δ is the sampling interval used for the FFT analysis and r is a random number between 0 and 1. The data were collected at different Δ values, always giving a total of 4096 data points. In a final step, white noise with a Gaussian distribution and variance of $\sigma^2 = 2$ was added to the function for all four sets of data.

The percentage error in detection of $f_1 = 0.05$ Hz is shown in Figure 3. A logarithmic scale is used to allow better resolution of the rapidly decreasing error as the number of cycles increases from one to six. When less than six cycles of f_1 are sampled, the accuracy of all methods is poor. The accuracy is slightly higher for the FFT (Figure 3a) at a constant sampling frequency than for a fixed number of points, but note that as the number of cycles increases, the gain in accuracy is constant, whereas the number of points and computational time increase as $M \log_2 M$, where M is the number of data points. In comparing the FFT, Lomb, and DFT results for 4096 data points (Figure 3b), the DFT continually improves in accuracy as the number of cycles sampled increases, but at a high computational cost of M^2 computations. The FFT error is constant at 2.3% after six cycles, with a low computational cost of $M \log_2 M$ computations. As expected, the accuracy of the Lomb method lies between the FFT and the DFT. Minima in the Lomb errors occur where either a bin frequency exactly coincides with f_1, or the sampling frequency is an exact multiple of f_1. For all cases, the Lomb algorithm outperforms the FFT in terms of accuracy of the frequency determination, and where the number of cycles sampled is greater than six, the accuracy is better than 1%. The computational time for the Lomb algorithm, $M \log_{10} M_f$, is substantially smaller than that for the DFT.

For flows close to the impeller in a stirred tank, the particle arrival rate is very high. This gives the user substantially more leeway in the choice of spectral analysis technique, because the signal is essentially continuous and can easily be resampled. In the region of interest for this work (close to the baffles and in the upper half of the tank) the particle arrival rate varies and can be substantially lower than that measured close to the impeller. The Lomb algorithm is selected for its ability to operate directly on the unevenly sampled data, and to accurately identify the dominant low frequencies in the signal.

Experimental Conditions

The flat-bottom cylindrical tank used in this work is shown in Figure 4a. In the center of the tank an impeller is mounted on the shaft. Four rectangular baffles of width $W = T/10$ are equally spaced around the tank wall. The geometric variables of interest are: the tank diameter, $T = 0.240$ m; the impeller diameter D; the off-bottom clearance C; and the liquid level H. For all experiments the liquid level H in the tank was kept equal to the tank diameter, $H = T$. The clearance and impeller diameter, C and D, were varied. To prevent air entrainment and surface vortexing, a lid was placed on the top of the tank, which was covered with an additional 2 cm of fluid to seal the shaft opening. The lid is known to have no effect on the mean velocity and it does not affect the main circulation (Ljungqvist and Rasmuson, 1998).

Three axial impellers were studied: a four-bladed 45°

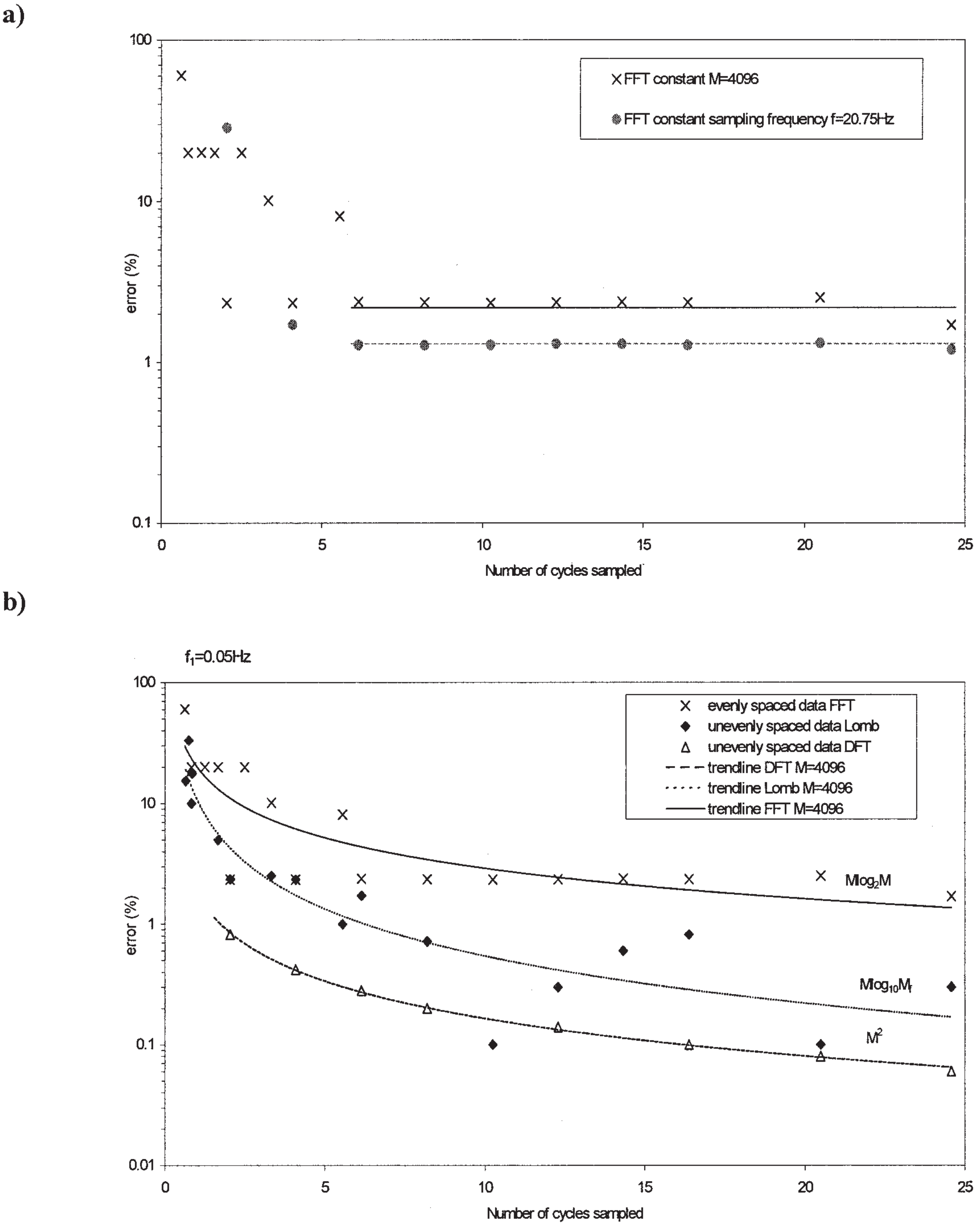

Figure 3. (a) Performance of FFT: constant M = 4096 vs. constant sampling frequency f = 20.75 Hz; (b) comparison between FFT, least-square Lomb method and direct Fourier transform (DFT) at constant M = 4096.

pitched-blade turbine (PBT), Lightnin fluidfoil impeller (A310), and a Chemineer high-efficiency impeller (HE3). All impellers are shown in Figure 5. The A310 and HE3 were used as supplied by Lightnin and Chemineer, respectively. Dimensions for the PBT impellers are given in Table 1.

The measurement locations, shown in Figure 4, were selected based on two considerations: the overall fluid circulation pattern and the known behavior of the circulation pattern macroinstability. The overall fluid circulation pattern in a stirred tank depends mainly on the type of impeller. In the case of an axial impeller the flow is directed toward the bottom of the tank. On the bottom the fluid diverges, changing its direction, and then travels upward along the vessel wall. Bittorf and Kresta (2001) showed that axial impellers drive four wall jets that propagate upward along the four baffles in the tank. The wall jets penetrate the bulk of the tank, involving two thirds of the tank volume in active circulation (Bittorf and Kresta, 2000). At the top of the tank the wall jets lose most of their

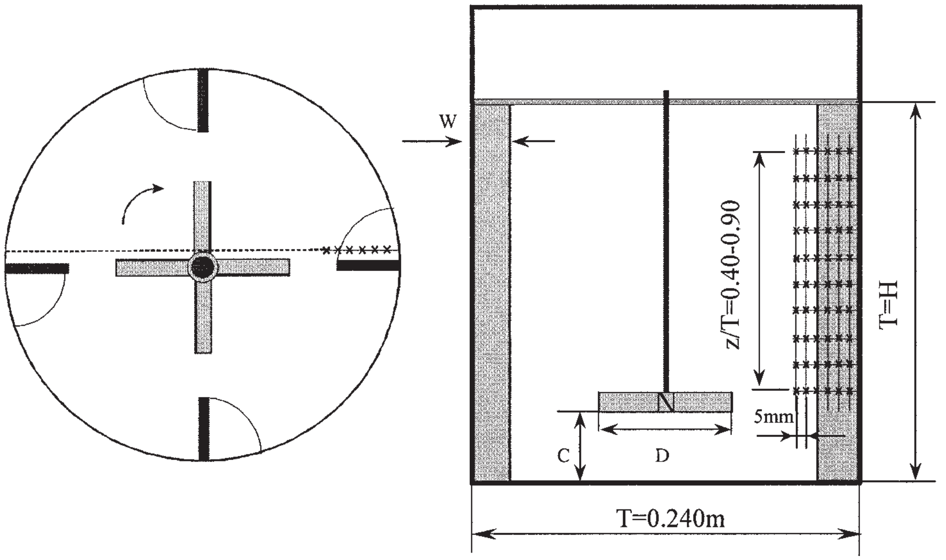

Figure 4. Geometry of the stirred tank and measurement locations.

axial momentum, the flow is redirected, and then is drawn into the impeller suction, closing the circulation loop. In the wall region, the BPF associated with the impeller blade passages has died out, but the velocities in the wall jets are still high enough to give good data rates and the macroinstabilities are actively propagating from the impeller discharge to the bulk of the tank.

The measurement grid was designed to cover the full height of the tank over the region where the circulation pattern macroinstabilities are dominant. The LDV measurements were done in a plane located 5 mm upstream of the baffle. This coincides with the region of formation of the three-dimensional wall jet (Bittorf and Kresta, 2001) and propagation of the macroinstability. Except for the case of the small-diameter PBT ($D = T/3$), a total of 60 grid points were examined: six points in the radial direction ($r = 90–115$ mm) at 10 axial traverses from $z/T = 0.40–0.90$ in 0.05 intervals, omitting the traverse at $z/T = 0.85$. For a small-diameter PBT ($D = T/3$), a total of 30 points were examined: six points at the same radial positions but at five widely spaced axial traverses ($z/T = 0.46$, 0.58, 0.71, 0.83, and 0.92). At each point in the grid, the velocity was sampled over a period that is long relative to the

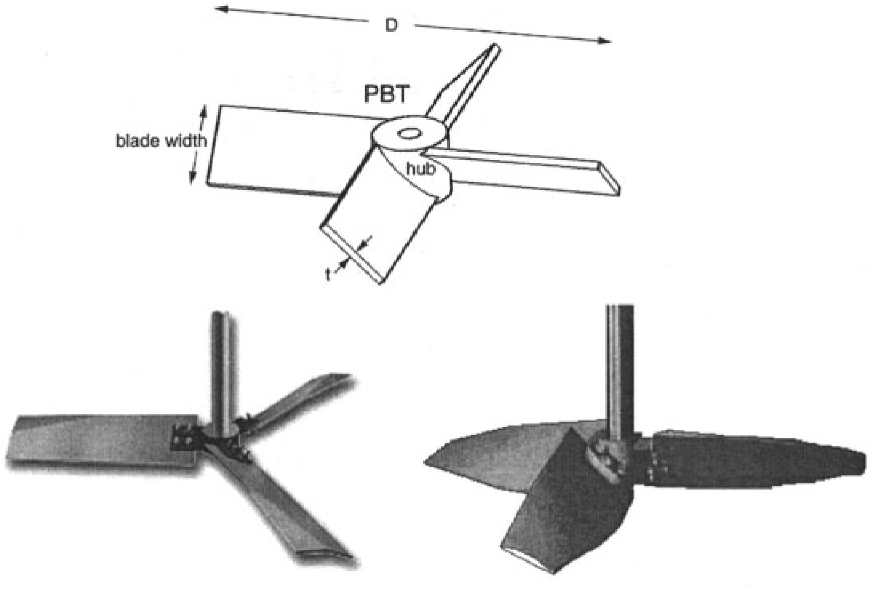

HE3 **A310**

Figure 5. 45° PBT impeller with diameter, *D* = *T*/2, high-efficiency impeller by Chemineer (HE3-axial flow) and fluidfoil A310 (by Lightnin).

Table 1. Impeller Dimensions in Millimeters

Impeller Type	$T/2$ PBT	$T/3$ PBT
Diameter, D	120	80
Hub diameter	22.2	15.9
Hub bore	6.4	6.4
Hub height	18.6	12.1
Blade thickness	2.44	0.61
Blade width	24.1	15.9

*From Chapple et al. (2002).

Table 3. Equipment Specifications of the Aerometrics LDV System Used in This Work

Parameter	Aerometrics LDV
Focal length, mm	500
Beam separation before expansion, mm	16.9
Beam intersection angle, °	3.87
Measuring volume diameter, μm	136.8
Measuring volume length, μm	1170
Fringe separation, μm	7.6
Number of fringes	18
Seeding particle diameter,* μm	1–3

*Naturally occurring particles in tap water.

expected frequency of the macroinstability and the Lomb method was used to extract the dominant frequencies.

The geometries selected for this study arise from the work by Chapple and Kresta (1994), who investigated the stability of the flow field using tuft visualization. They showed that the stability of the flow direction depends on a complex interaction between the impeller diameter (D) and off-bottom clearance (C). A bigger impeller diameter is more likely to interact with the vessel walls. On the other hand, Kresta and Wood (1993b) observed that the characteristics of the 45° PBT flow field depend strongly on the off-bottom clearance. Instead of a single circulation loop that extends over the whole tank for all geometries, Kresta showed that the primary circulation loop reaches the bottom of the tank only for a $C = T/3$ clearance. When the clearance is increased to $C = T/2$, a secondary circulation loop forms in the bottom third of the tank. This motivated us to examine two impeller diameters and to cover three off-bottom clearances. Table 2 details all geometries examined.

The limit of fully turbulent flow for the impeller (based on the power number curve and similarity scaling of velocity profiles at the impeller) is a Reynolds number equal to 2×10^4. Below $\mathrm{Re} = 2 \times 10^4$ the flow is transitional. The Reynolds number was adjusted by changing both the fluid viscosity ν and the impeller rotational speed N. This provides an opportunity to study how the macroinstability responds to a change in the ratio between the viscous and inertial forces over almost two orders of magnitude. This is especially important in the bulk of the tank where the macroinstability persists while the turbulence is suppressed (Roussinova and Kresta, 2000).

The working fluids selected are all Newtonian: water, Bayol-35, and solution of triethylene glycol (TEG) in water. The fluids and their viscosities are summarized in Table 2. For the viscosity of water, literature values are used, whereas for Bayol-35 and water solutions of TEG these values were measured. The fluid viscosity for TEG solutions was measured using a Cannon–Fenske viscometer at room temperature. Because of intense agitation, a slight change (up to 2°C) of the fluid temperature in the tank was observed. For all experiments the viscosity of TEG was monitored and Reynolds numbers were determined based on the average viscosity. In the worst case (TEG solution with highest viscosity), an increase in temperature of 2°C will change the kinematic viscosity no more than 3×10^{-6} m^2/s. Thus the relative error in Reynolds number attributed to temperature variation does not exceed 10%.

The velocity time series were measured using a one-component Aerometrics LDV system. An argon ion laser ($\lambda = 514.5$ nm, 300 mW) was operated in forward-scatter mode. Further details of the instrument configuration are given in Zhou and Kresta (1996). The optical parameters are specified in Table 3.

An Aerometrics Doppler signal analyzer (DSA) was used to convert the analog signal from the receiving optics into Doppler frequencies and to obtain the velocity time series. The DSA operates in the frequency-domain burst-detection mode. For all experiments the analog signal was sampled at 2.5 or 5 MHz. These frequencies were shown to be optimum for determination of the mean and RMS velocities by Zhou and Kresta (1996), Grgic (1998), and Bittorf and Kresta (2000). Selection of either fixed sampling size (number of velocity measurements) or fixed sampling time (length of record in seconds) is required. Table 2 lists the parameters selected for all runs. In the impeller region, the data collection is faster than that in the top of the tank because the fluid velocity is higher and more fluid traverses the measuring volume per unit time. The particle arrival rate at the top of the tank also varies depending on the Reynolds number. If the impeller operates at 400 rpm and the number of samples is fixed (such as at 8000), then the acquired

Table 2. Experimental Runs Studied Combined with the Settings of the Doppler Signal Analyzer (DSA)

Geometrical Parameters ($T = 0.240$ m)					Doppler Signal Analyzer Parameters		
Impeller Type	Impeller Diameter, D	Clearance, C/D	N (rpm)	Fluid*	Number of Samples	Sampling Time (s)	Number of f_{MI} Cycles
45° PBT	$T/2$	0.33, 0.50, 0.67	200	Water (1.0)	8000	20–45	12.4–28
	$T/2$	0.50	400	Water (1.0)	60,000–100,000	60	74.4
	$T/2$	0.50	250, 300, 450	Bayol-35 (3.0)	60,000–100,000	60	46.5, 55.8, 83.7
	$T/2$	0.50	570	TEG-1 (9.0)	60,000–100,000	60	106
	$T/2$	0.50	300, 400, 500, 600	TEG-2 (23.0)	60,000–100,000	60	60, 80, 100, 120
	$T/3$	0.50, 1.0	563	Bayol-35 (3.0)	40,000–80,000	50	N/A
A310	0.58 T	0.33, 0.50, 0.67	200	Water (1.0)	8000	20–45	N/A
HE3	$T/3$	0.40, 0.80, 1.0	400	Water (1.0)	8000	15–30	N/A

*Values of kinematic viscosities relative to the viscosity of water (1×10^{-6} m^2/s) are given in parentheses.

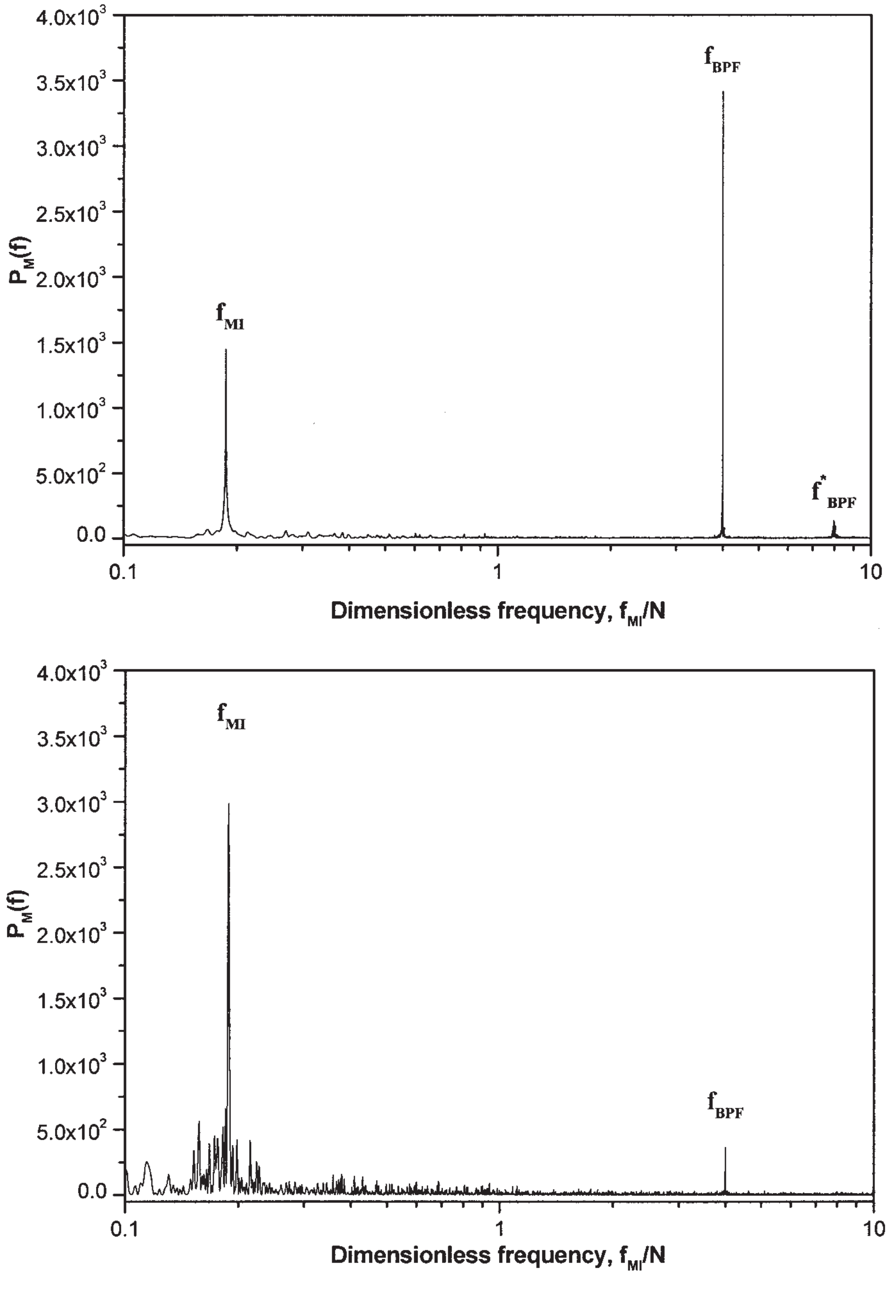

Figure 6. (a) Lomb frequency spectrum for the axial velocity at 2*r*/*D* = 1.05 and *z*/*T* = 0.60 showing peaks attributed to the BPF and MI. Note that f_{MI} = 1.77 Hz (45° PBT, *C*/*D* = 0.5, and *D* = *T*/2, TEG-1, Re = 15,200, *N* = 570 rpm); (b) Lomb frequency spectrum for the axial velocity at 2*r*/*D* = 1.35 and *z*/*T* = 0.60 showing peak attributed to the MI and dramatic decay of the power at the BPF. Note that f_{MI} = 1.77 Hz (45° PBT, *C*/*D* = 0.5, and *D* = *T*/2, TEG-1, Re = 15,200, *N* = 570 rpm).

time series will contain the same amount of data as for the case of 200 rpm, but the total time will be much shorter. This becomes important for the HE3 and A310 impellers, which require much longer sampling times than the PBT. For all measurements the particle arrival rate (or data rate) varied from 1500 to 500 Hz and the percentage of validated samples was higher than 99%.

A computer-driven traverse was used to position the tank in the two horizontal directions: *x* and *y*. Positioning in the vertical direction and off-bottom clearance adjustments for the impeller were done manually. The positioning accuracy of the horizontal *x*- and *y*-traverses was ±0.25 mm, whereas the vertical traverse accuracy was ±0.5 mm.

Results

The frequency spectra of the axial velocity time series throughout the measurement grid were calculated using the Lomb algorithm. The Lomb spectrum in Figure 6a shows the presence of both the BPF (blade passage frequency) and the macroinstabilities, but such spectra are typical only for locations close to the impeller. There is a clear, 20-fold separation in scales between the BPF and the observed low frequency, suggesting that the macroinstabilities are more closely related to the mean flow than to the turbulence. The BPF almost disappears from the spectrum by a radial position of $2r/D = 1.35$, as shown in Figure 6b. Note that the peak attributed to the macroinstability is very clearly defined for the Lomb algorithm, whereas previously reported spectra based on the FFT of sample and hold data give a broad band for the low frequency.

The repeatability of the measured frequency was assessed by finding the pooled variance for five replicates of each of four experiments. The standard deviation of the raw frequency was 0.025 Hz. When the frequencies are normalized with N, the dimensionless standard deviation is 0.005.

At each measurement location in the grid, the frequencies containing power higher than 75% of the maximum peak in the spectrum were identified as the dominant frequencies. Because all time series have finite length, the lowest possible frequency was calculated in such a way that the total time interval could sustain at least five periods. All frequencies lower than this limit were discarded.

To evaluate the coherence of the dominant frequencies, the results for the full measurement grid were combined in a histogram for each of the 11 geometries investigated. The histogram bin size was selected to include enough counts for statistics (the bin size is one order of magnitude larger than the spectral resolution of Lomb method) while maximizing the resolution of the histogram. To allow direct comparison of the results for all impellers the bin size was fixed at a dimensionless frequency of 0.0150 and the y-axis scale was fixed at the total number of measurement grid points. For the hydrofoil impellers, the dominant low frequencies were not coherent. For the small-diameter PBT, the dominant low frequencies were in good agreement with previous studies, but there was no single resonant geometry for a circulation pattern macroinstability. For the large-diameter PBT, a single resonant geometry with a very coherent circulation pattern macroinstability frequency was identified. The frequency scales exactly with rotational speed over a large range of Reynolds numbers, and can be related to resonant frequencies for other impinging jet geometries.

HE3 and A310

Roussinova et al. (2000) previously showed that the low frequencies associated with HE3 and A310 impellers are characterized by small amplitudes and very slow variations. The amplitude is comparable to the amplitude of the turbulent fluctuations, which provides a severe challenge for frequency analysis. Accurate frequency analysis of such signals requires a very long record with multiple frequency cycles.

The frequency histograms for the Chemineer HE3 impeller ($D = T/3$, Re = 42,666) at three different clearances are shown in Figure 7. For all clearances, the total count of frequencies that exceed the 75% threshold is also shown. The total frequency counts indicate the average number of dominant frequencies calculated per measurement. For the HE3 impeller (60 measurement points and 120 or more counts) the total counts suggest that at every point at least two frequencies appear simultaneously, scattered randomly in the low-frequency range. No single frequency is observed over more than 30% of the grid. In some runs, with very intermittent signals, the Lomb analysis approaches the limit where the statistically significant peak cannot be distinguished from the background turbulence. These points usually occur in the upper axial traverses at a radial position of $r = 95$ mm, coincident with the baffle. This measurement location is in the wake of the baffle where the flow changes direction rapidly. The histograms show no coherent macroinstability frequency; on the contrary, a broad band of low frequencies is evident. These results confirm earlier qualitative observations of hydrofoil impellers by Jaworski et al. (1996).

In Figure 8 the frequency histograms for the A310 are shown. The impeller diameter in this case is $D = 0.58T$. The Reynolds number is Re = 64,588, so again the flow field is fully turbulent. Once again, the dominant frequencies are unstable, with the dimensionless frequency f_{MI}/N ranging from 0.09 to 0.132. The total counts show that, on average, two frequencies are significant for every measurement. Unlike the HE3, the A310 histograms show a peak close to $0.10N$ for all clearances. This peak is not deemed coherent for two reasons. First, the peak is present only for roughly half the grid points; second, the amplitude of the macroinstability fluctuations is very small (Roussinova et al., 2000) and comparable to the size of the turbulent fluctuations. The maximum variability of the frequencies is observed in the case $C/D = 0.33$, where a total of 201 frequencies exceed the threshold level (more than three frequencies at each point). The flow pattern in this configuration is influenced by the proximity of the impeller to the tank bottom. This gives rise to a wide distribution of frequencies because there is interaction between the impinging flow at the bottom of the tank and the impeller discharge.

Additional macroinstabilities generated by this impeller may have a very long period, of the order of *few hundred* impeller rotations, as indicated by the small peak at $0.03N$. The long period of A310 macroinstabilities and their relatively small amplitude compared to the amplitude of the macroinstabilities generated by PBT require very long velocity time records. The records would have to be extended up to 5–10 min to obtain more closely defined results.

45° PBT: small diameter D = T/3

In this set of experiments the small diameter PBT ($D = T/3$) was examined at Re = 20,622 for two off-bottom clearances, $C/D = 0.5$ and 1.0. Figure 9 shows the distribution of dominant frequencies from 30 measurement locations. Two low frequencies, $f = 0.015N$ and $0.065N$, appear over at least two thirds of the measurement grid. These frequencies were previously reported by Bruha et al. (1993; $f = 0.06N$) and more recently by Nikiforaki et al. (2003; $f = 0.02N$).

Bruha et al. (1993) quantified a frequency that they associated with the vortex breakup by monitoring the deformation of the liquid surface for a small PBT impeller at an off-bottom clearance $C/D = 1.0$. They found that this process happens regularly with a low frequency of $f = 0.06N$. The vortex disintegration was always located between two baffles, the same area where the frequency appears on our measurement grid. More recently, Nikiforaki et al. (2003) reported a very

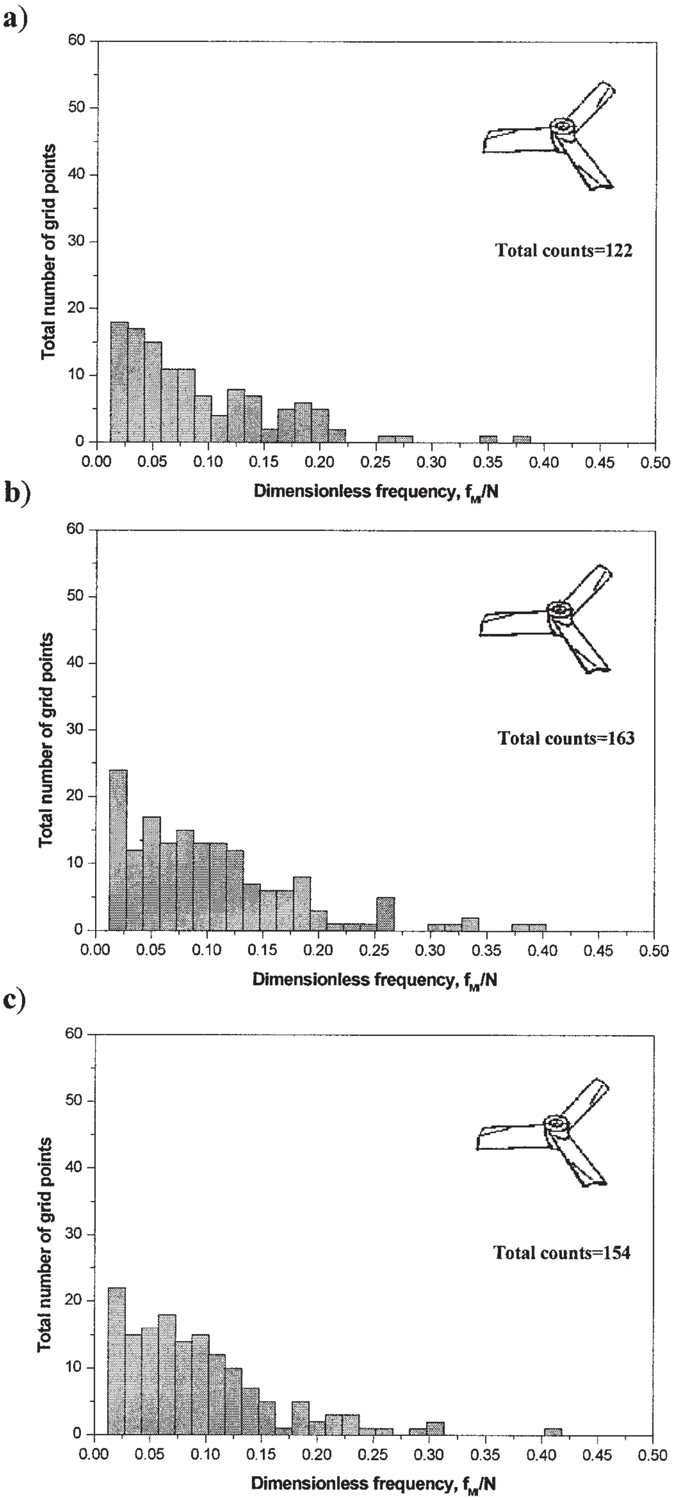

Figure 7. Distribution of frequencies for HE3 with constant impeller diameter, $D = T/3$, Re = 42,666, N = 400 rpm, 60 points in measurement grid and three C/D ratios: (a) 0.40, (b) 0.80, and (c) 1.0.

low macroinstability frequency of 0.015–0.02N in the same geometry, apparently the result of a precessing vortex.

At the lower clearance, C/D = 0.50, the same frequencies appear. The lower frequency, $f = 0.015N$, appears over 70% of the measurement grid, and at all points in the upper traverses (z/T = 0.83, 0.92). This supports the hypothesis that this low frequency is attributed to the convection of a precessing vortex revolving around the impeller shaft. The second frequency, $f = 0.065N$, was observed over 90% of the grid in all of the lower traverses (z/T = 0.46–0.71) from the edge of the baffle to the

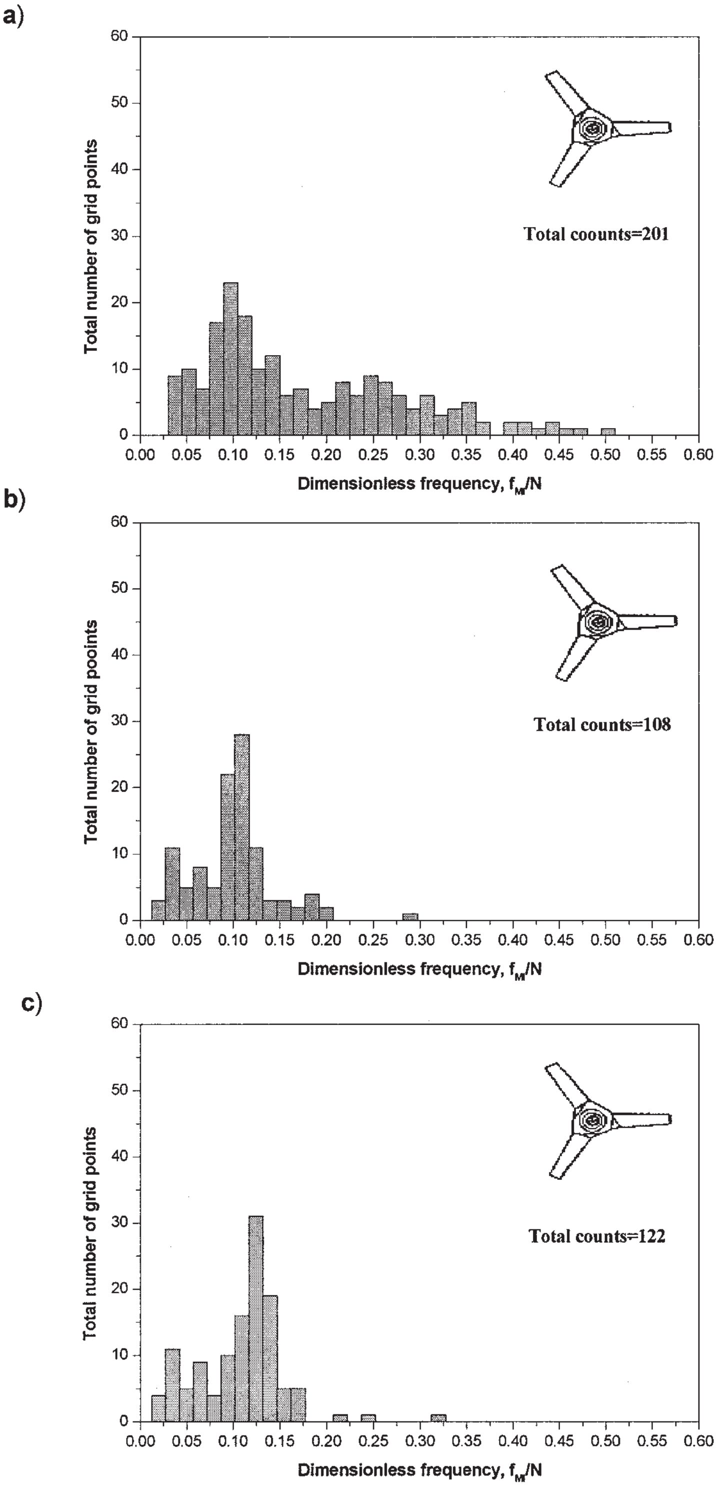

Figure 8. Distribution of frequencies for A310 with constant impeller diameter, $D = 0.58T$, Re = 64,588, N = 200 rpm, 60 points in measurement grid and three C/D ratios: (a) 0.33, (b) 0.50, and (c) 0.67.

tank wall. There are two plausible explanations for this frequency. One is that a vertical vortex is shed periodically from the baffle. This vortex may then travel toward the shaft where it is convected tangentially, becoming the very low frequency of precessing vortex observed by Nikiforaki et al. (2003). The other possibility, proposed by Bruha et al. (1993), is that trailing vortices periodically escape from the impeller region and travel to the fluid surface. The tangential component of velocity constrains the path of the vortex to the space between the baffle and the wall of the tank. Although both hypotheses are plausible, more research would be needed to systematically explain the origin of these two frequencies.

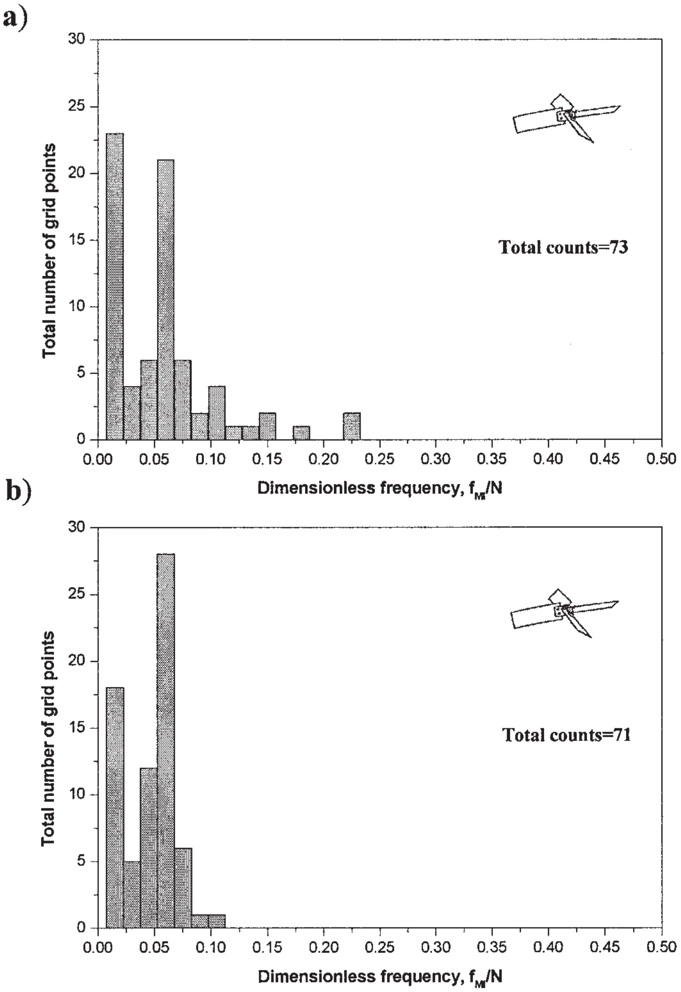

Figure 9. Distribution of frequencies for 45° PBT with constant impeller diameter, *D* = *T*/3, Re = 20,622, 30 points in measurement grid and two *C*/*D* ratios: (a) 0.50, (b) 1.0.

45° PBT: large diameter D = T/2

For a large-diameter 45° PBT, $D = T/2$, and Re = 48,000, the distribution of frequencies is shown in Figure 10. There is a distinctive peak at a frequency of $f_{MI} = 0.186N$. This frequency remains dominant when the *C*/*D* ratios are varied, but for *C*/*D* ratios 0.33 and 0.67, the histograms show the presence of additional frequencies $f^* = 0.075N$ and $f^{**} = 0.26N$ and some scattered minor frequencies. The resonant geometry for the macroinstabilities is clearly $D = T/2$, $C/D = 0.5$ (Figure 10b). At this off-bottom clearance the dominant frequency is identified as 0.186*N* and for 80% of the points 0.186*N* is the only significant frequency. In this geometry one frequency is both coherent (extending over the full measurement grid) and resonant (the single dominant frequency).

Once the dominant macroinstability frequency and resonant geometry were determined, the experiments were extended by varying the fluid viscosity. The scaling of the dimensionless macroinstability frequency f_{MI}/N with Reynolds number is shown in Figure 11. For $\text{Re} > 2 \times 10^4$ the dimensionless frequency is constant at 0.186. Large-eddy simulations and large-scale experiments (Roussinova et al., 2003) returned the same results.

The driving mechanism for the circulation pattern macroinstability can be explained by considering the interaction of the impeller discharge stream with the walls of the tank. In the resonant geometry, the impeller discharge stream meets the walls of the tank exactly in the bottom corner of the tank. This can be described as a confined impinging jet, a flow for which a substantial body of literature exists. Impinging jets are used to generate resonant frequencies in many musical instruments. They are used for mixing in impinging jet mixheads. They can also generate strong resonant and destructive vibrations in the context of VSTOL (vertical or short takeoff and landing) aircraft applications. The literature on the fundamental mechanisms driving these flows is extensive, and dates back to 1861. Blake and Powell (1986) and Rockwell and Naudascher (1979) provide extensive reviews.

Impinging jet literature conclusively shows that the mechanism driving coherent frequencies resulting from jet impingement is a feedback loop. The jet, which is an unstable free shear layer, impinges on a wall. The interaction with the wall produces a pressure wave, which is reflected back upstream. This pressure wave excites instabilities in the free shear layer, which are further reinforced by feedback from the pressure wave at

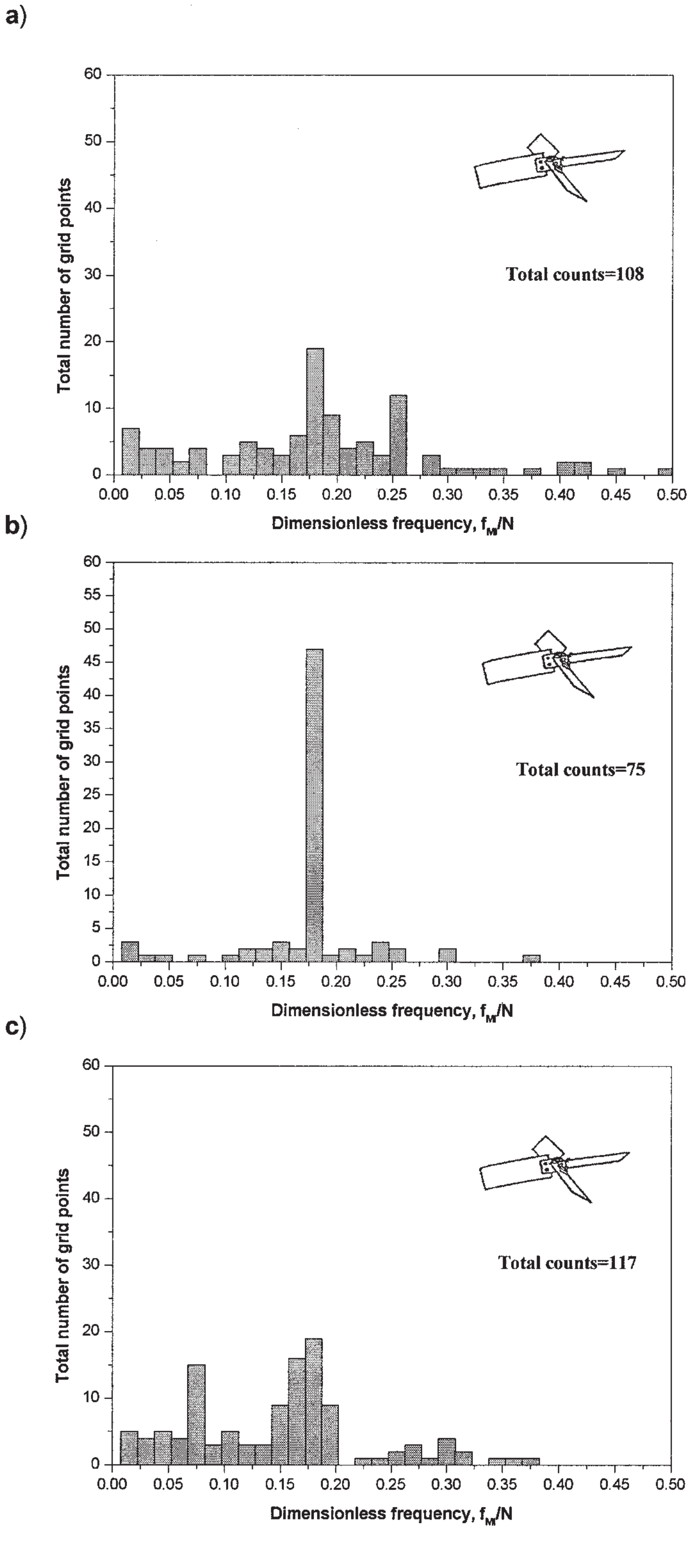

Figure 10. Distribution of frequencies for 45° PBT with constant impeller diameter, *D* = *T*/2, Re = 48,000, 60 points in measurement grid, and three *C*/*D* ratios: (a) 0.33, (b) 0.50, and (c) 0.67.

the impingement surface, which begins to oscillate in response to the shear layer instability. Recent papers by Ho and Nossier (1981) and Zaida (1995) illustrate the mechanism very clearly. Zaida (1995) successfully implemented feedback control of the frequency, providing conclusive proof of the mechanism of excitation. The quantitative relationship of the circulation pattern macroinstability to other impinging jet resonant frequencies is discussed in Roussinova et al. (2003).

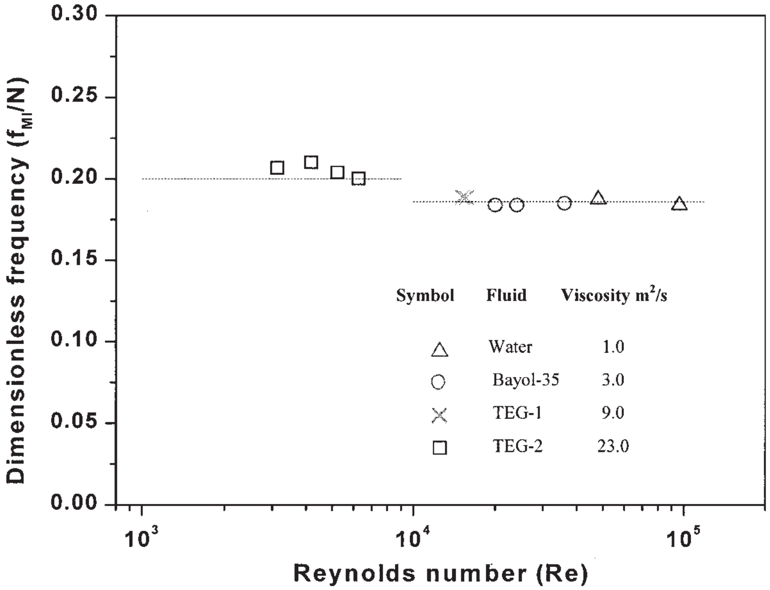

Figure 11. Scaling of the dimensionless frequency for the resonant geometry: 45° PBT, *D* = *T*/2, *C*/*D* = 0.50.

Conclusions

LDV time series of axial velocities upstream of the baffle in a stirred tank were successfully analyzed using the Lomb algorithm, which is more accurate than the FFT and can be applied to unevenly spaced data. The Lomb algorithm was able to correctly capture the dominant frequencies in the flow. The observed frequencies are 20 times lower (large-diameter PBT, $D = T/2$) and even 200 times lower (small-diameter PBT, $D = T/3$) than the characteristic blade passage frequency (BPF). These frequencies are clearly associated with the presence of different large-scale flow macroinstabilities related to an unsteady mean flow rather than the turbulent cascade. The timescale of the observed macroinstabilities is of the order of the tank turnover time and can have significant implications for mechanical design of stirred tanks.

The purely axial impellers examined, HE3 and the A310, did not show any coherent frequency. Any macroinstabilities generated by HE3 and A310 impellers have a very long timescale and very small amplitude compared to the macroinstabilities generated by the PBT.

The frequency analysis for a small-diameter 45° PBT ($D = T/3$) also revealed coherent low frequencies. One of these frequencies is attributed to a precessing vortex and its frequency, $f = 0.015N$, is close to that reported by Nikiforaki et al. (2003). This frequency matches the convection velocity of a forced vortex centered on the impeller shaft. The second frequency, $f = 0.065N$, was also observed by Bruha et al. (1993) in their "surface swelling" experiments. No single mechanism could be isolated for this frequency.

For the large-diameter 45° PBT ($D = T/2$) a single resonant frequency of the circulation macroinstability, $f_{MI} = 0.186N$, was observed. This frequency remains dominant when the off-bottom clearance (C/D) is changed but is less coherent. Two minor frequencies appear ($f^* = 0.075N$ and $f^{**} = 0.26N$) and there is a distribution of other frequencies around the dominant peaks. In the resonant geometry ($D = T/2$, $C/D = 0.50$) the frequency of the macroinstability scales linearly with the rotational speed of the impeller N, for Reynolds numbers from 20,000 to 100,000. This coherent frequency with a single resonant geometry was related to the impingement of the impeller discharge stream on the bottom corner of the tank. Where tanks are designed using this particular geometry, additional care must be taken with the mechanical stability of the vessel.

Acknowledgments

The authors thank both the Natural Sciences and Engineering Research Council of Canada (NSERC) and Lightnin for financial support of this work. We also thank Dr. Kevin Bittorf and Vera Knesic for providing the experimental data used in this work.

Notation

a = parameter
A = constant
b = parameter
$b_i(t)$ = orthonormal basis function, Fourier kernel
c = constant
C = impeller off-bottom clearance, m
CC, CS = Lomb notation
D = impeller diameter, m
E = mean square energy
f = frequency, Hz
f_{BPF} = frequency of BPF, Hz
f_{c} = Nyquist frequency, Hz
f_{MI} = frequency of macroinstability, Hz
f_{PV} = frequency of the precessing vortex, Hz
i = index of summation
j = square root of -1
k = index of summation
M = number of data points
M_{f} = number of frequencies
N = impeller rotational speed, rpm or s^{-1}
P = general definition of a signal power
$P_M(f)$ = Lomb-normalized periodogram
r = radial position, m
r = radius of the shaft, m
R = radius of the outer cylinder, m
Re = impeller Reynolds number, ND^2/ν
s = wavenumber or scale

SS = Lomb notation
t = time, s
T = tank diameter, m
V_θ = velocity, m/s
x = continuous signal
$x_f(t)$ = continuous wave
x_m = signal or time series with zero mean
x_m^* = complex conjugate
XC, XS = Lomb notations

Greek letters

Δ = sampling interval, T_{total}/M, s
δ_{ik} = Dirak delta function
ε_m = error
λ_{max} = Lyaponov exponent
ν = kinematic viscosity, m^2/s
π = pi constant
ρ = fluid density, kg/m^3
σ = constant
τ = time delay
$\psi(x)$ = wavelet

Abbreviations

ACF = autocorrelation function
A31 = three-bladed aerofoil impeller by Lightnin
BPF = blade passage frequency
DFT = discrete Fourier transform
DTFT = discrete time Fourier transform
DPIV = digital particle image velocimetry
FFT = fast Fourier transform
HE3 = three-bladed high-efficiency turbine by Chemineer
MI = macroinstability
LDV = laser Doppler velocimeter
PBT = four-bladed, 45° pitched-blade turbine
POD = proper orthogonal decomposition
RMS = root mean square

Literature Cited

Antonia, R. A., and D. Britz, "A Comparison of Methods of Computing Power Spectra from LDV Signals," *Meas. Sci. Technol.*, **7**, 1024 (1996).

Bakker, A., and J. B. Fasano, "Stirred Tank Flow Pattern Study Using Digital Particle Image Velocimetry," Proc. of the 1995 AIChE Annual Meeting, Nov. 1995, Miami Beach Session 123, Paper No. 123c (1995).

Benedict, L. H., H. Nobach, and C. Tropea, "Estimation of Turbulent Velocity Spectra from Laser Doppler Data," *Meas. Sci. Technol.*, **11**, 1089 (2000).

Bird, R. B., W. E. Stewart, and E. Lightfoot, *Transport Phenomena*, 2nd Edition, Wiley, Hoboken, NJ (2002).

Bittorf, K., "The Application of Wall Jets in Stirred Tanks with Solids Distribution," PhD thesis, University of Alberta, Edmonton, Canada (2000).

Bittorf, K., and S. M. Kresta, "Three-Dimensional Wall Jets: Axial Flow in a Stirred Tank," *AIChE J.*, **47**(6), 1277 (2001).

Bonnet, J. P., J. Delville, M. N. Glauser, and R. A. Antonia, "Collaborative Testing of Eddy Structure Identification Methods in Free Turbulent Shear Flow," *Exp. Fluids*, **25**, 197 (1998).

Bruha, O., I. Fort, and P. Smolka, "Large Scale Unsteady Phenomenon in a Mixing Vessel," *Acta Polytech. Czech Tech. Univ. Prague*, **27**, 33 (1993).

Bruha, O., I. Fort, and P. Smolka, "Flow Transition Phenomena in an Axially Agitated System," Proc. of the VIII European Conf. on Mixing (IChemE Symposium Series, Cambridge, UK), Vol. 136, p. 121 (1994).

Bruha, O., I. Fort, and P. Smolka, "Phenomenon of the Turbulent Macroinstabilities in Agitated Systems," *Collect. Czech. Chem. Commun.*, **60**, 85 (1995).

Bruha, O., I. Fort, P. Smolka, and M. Jahoda, "Experimental Study of Turbulent Macroinstabilities in an Agitated System with Axial High-Speed Impeller and with Radial Baffles," *Collect. Czech. Chem. Commun.*, **61**, 856 (1996).

Chapple, D., and S. M. Kresta, "The Effect of Geometry on the Stability of Flow Patterns in Stirred Tanks," *Chem. Eng. Sci.*, **49**(21), 3651 (1994).

Chapple, D., S. M. Kresta, A. Wall, and A. Afacan, "The Effect of Impeller and Tank Geometry on Power Number for a PBT," *Trans. IChemE A*, **80**, 364 (2002).

Drain, L. E., *The Laser Doppler Technique*, Wiley, Toronto (1980).

Durst, F., A. Melling, and H. J. Whitelaw, *Principles and Practice of Laser Doppler Anemometry*, 2nd Edition, Academic Press, New York (1981).

Farge, M., "Wavelet Transforms and Their Applications to Turbulence," *Annu. Rev. Fluid Mech.*, **24**, 395 (1992).

Gaster, M., and J. B. Roberts, "Spectral Analysis of Randomly Sampled Signals," *J. Inst. Math. Appl.*, **15**, 195 (1975).

Gaster, M., and J. B. Roberts, "The Spectral Analysis of Randomly Sampled Records by Direct Transform," *Proc. R. Soc. London A*, **354**, 27 (1977).

Grgic, B., "Influence of the Impeller and Tank Geometry on Low Frequency Phenomena and Flow Stability," MS Thesis, University of Alberta, Edmonton, Canada (1998).

Hasal, P., J.-L. Montes, H.-C. Boisson, and I. Fort, "Macroinstabilities of Velocity Field in Stirred Vessel: Detection and Analysis," *Chem. Eng. Sci.*, **55**, 391 (2000).

Horne, J., and S. Baliunas, "A Prescription for Period Analysis of Unevenly Sampled Time Series," *Astrophys. J.*, **302**, 757 (1986).

Houcine, I., E. Plasari, R. David, and J. Villermaux, "Feedstream Jet Intermittency Phenomena in Continuous Stirred Tank Reactor," *Chem. Eng. J.*, **72**, 19 (1999).

Jaworski, Z., A. Nienow, and K. Dyster, "An LDV Study of the Turbulent Flow Field in a Baffled Vessel Agitated by Axial, Down-Pumping Hydrofoil Impeller," *Can. J. Chem. Eng.*, **74**, 3 (1996).

Kresta, S. M., "Turbulence in a Stirred Tank: Anisotropic, Approximate and Applied," Can. J. Chem. Eng., **76**(3), 563 (1998).

Kresta, S. M., and V. T. Roussinova, "Comments to 'On the Origin, Frequency and Magnitude of Macroinstabilities of the Flows in Stirred Vessels' by Nikiforaki et al.," *Chem. Eng. Sci.*, **59**(4), 951 (2004).

Kresta, S. M., and P. E. Wood, "The Flow Field Produced by a Pitched Blade Turbine: Characterization of the Turbulence and Estimation of the Dissipation Rate," *Chem. Eng. Sci.*, **48**, 1761 (1993a).

Kresta, S. M., and P. E. Wood, "The Mean Flow Field Produced by a 45° Pitched Blade Turbine: Changes in the Circulation Pattern due to Off-bottom Clearance," *Can. J. Chem. Eng.*, **71**, 42 (1993b).

Ljungqvist, M., and A. Rasmuson, "A Comparison of the Hydrodynamics of Open and Closed Vessels," *Chem. Eng. Commun.*, **165**, 123 (1998).

Lomb, N. R., "Least-Squares Frequency Analysis of Unequally Spaced Data," *Astrophys. J.*, **39**, 447 (1976).

Mayo, W. T., "A Discussion of Limitations and Extensions of Power Spectrum Estimation with Burst Counter LDV Systems," Proc. of the 2nd Int. Workshop on Laser Velocimetry, Purdue University, West Lafayette, IN, pp. 90–104 (1974).

Montes, J. L., H. C. Boisson, I. Fort, and M. Jahoda, "Velocity Field Macro-Instabilities in an Axial Agitated Mixing Vessel," *Chem. Eng. J.*, **67**, 139 (1997).

Muller, E., H. Nobach, and C. Tropea, "Model Parameter Estimation from Non-Equidistant Sampled Data Sets at Low Data Rates," *Meas. Sci. Technol.*, **9**, 435 (1998).

Myers, K. J., R. W. Ward, and A. Bakker, "A Digital Particle Image Velocimetry Investigation of Flow Field Instabilities of Axial Flow Impellers," *J. Fluids Eng.*, **119**, 623 (1997).

Nikiforaki, L., G. Montante, K. Lee, and M. Yianneskis, "On the Origin, Frequency and Magnitude of Macroinstabilities of the Flows in Stirred Vessels," *Chem. Eng. Sci.*, **58**(13), 2937 (2003).

Oppenheim, A. V., and A. S. Willsky, *Signal and Systems*, Prentice-Hall, Englewood Cliffs, NJ (1983).

Press, W. H., B. P. Flannery, S. A. Teukolsky, and W. T. Vetterling, *Numerical Recipes: The Art of Scientific Computing*, Cambridge University Press, New York (1989).

Roussinova V., B. Grgic, and S. M. Kresta, "Study of Macroinstabilities in Stirred Tanks Using a Velocity Decomposition Technique," *Trans. IChemE A*, **78**, 1040 (2000).

Roussinova, V., and S. M. Kresta, "Analysis of Macro-instabilities (MI) of the Flow Field in a Stirred Tank Agitated with Axial Impellers," Proc. of 10th European Conf. on Mixing, Elsevier Science, Delft, The Netherlands (2000).

Roussinova, V., S. M. Kresta, and R. Weetman, "Low Frequency Macroinstabilities in a Stirred Tank: Scale-up and Prediction Based on Large Eddy Simulations," *Chem. Eng. Sci.,* **58**(11), 2297 (2003).

Scargle, J., "Studies in Astronomical Time Series Analysis. II. Statistical Aspect of Spectral Analysis of Unevenly Spaced Data," *Astrophys. J.*, **263**, 835 (1982).

van Maanen, H. R. E., "Retrieval of Turbulence and Turbulence Properties from Randomly Sampled Laser-Doppler Anemometry Data with Noise," PhD Thesis, Delft University of Technology, The Netherlands (1999).

Winardi, S., S. Nakao, and Y. Nagase, "Pattern Recognition in Flow Visualization around a Paddle Impeller," *J. Chem. Eng. Jpn.*, **21**, 503 (1988).

Zhou, G., and S. M. Kresta, "Impact of the Tank Geometry on the Maximum Turbulence Energy Dissipation Rate for Impellers," *AIChE J.*, **42**, 2476 (1996).

Appendix

The Lomb least square method is based on general transformation theory (Oppenheim and Willsky, 1983), which shows that the projection of the signal $x(t)$ onto the element of an orthonormal basis, $b_i(t)$, is the value c, which minimizes the mean square error energy E. E is the integral of the squared differences between $x(t)$ and $cb_i(t)$ over the definition interval. The Lomb method implements this minimization procedure over the unevenly distributed sampled values of $x(t)$, considering that the basis functions are the Fourier kernel $b_i(t) = \exp(j2\pi f_i t)$.

Suppose that x_m is a discrete representation $x_m = x(t_m)$ ($m = 1, \ldots, M$) of a continuous signal x, and $b_i(t)$ is an orthogonal basis set, which defines the transform by

$$x = \sum_i c_i b_i(t) \tag{A1}$$

Multiplying both sides of Eq. A1 by $b_k(t)$ and integrating over t gives

$$\int_{-\infty}^{+\infty} x b_k(t)dt = \sum_i \int_{-\infty}^{+\infty} c_i b_i(t) b_k(t) dt \tag{A2}$$

For the righthand side (RHS) of Eq. A2, by applying the orthogonality condition given as $\int_{-\infty}^{+\infty} b_i(t) b_k(t)dt = \delta_{ik}$, we obtain

$$\text{RHS} = \sum_i c_i \int_{-\infty}^{+\infty} b_i(t) b_k(t)dt = \sum_i c_i \delta_{ik} = c_k \tag{A3}$$

The coefficients c_k that represent the x in the transformation domain are thus given as

$$c_k = \int_{-\infty}^{+\infty} x b_k(t) dt \tag{A4}$$

In Eq. A4 the continuous signal x needs to be replaced by the discrete values of the real signal x_m. Thus, the squared difference error E can be defined as the difference between the true signal x_m and its transformed value

$$E = \sum_m \varepsilon_m^2 = \sum_m \left[x_m - \sum_i c_i b_i(t_m) \right]^2 \tag{A5}$$

The constant coefficients c_i are those that minimize the squared error in Eq. A5. In the case of evenly sampled data in the Fourier domain, Eq. A5 is known as the discrete time Fourier transform (DTFT), its discretely evaluated version as DFT, and the associated fast algorithm used to compute it as the FFT. When the signal is available only at unevenly spaced time instants, one solution is proposed by Lomb (1976), who estimated the harmonic content by fitting, in the least-square sense, sine waves directly to the data. In the original work, Lomb introduces a time delay τ, at the basis or phase shift, which facilitates a better statistical description of the least-square spectrum estimate. Thus the generalized model for a given sine wave is adjusted as

$$x_f(t) = a_f \cos 2\pi f(t - \tau_f) + b_f \sin 2\pi f(t - \tau_f) \tag{A6}$$

In what follows the data are fit with a sine wave at a given frequency f. For clarity we are going to omit the subscript f from Eq. A6, pointing out that the least-square procedure needs to be repeated for every frequency selected.

The general idea is to seek the proper a and b parameters in such a way that the square difference functional E (Eq. A5) between the model (Eq. A6) and the signal is minimized:

$$E(a, b) = \sum_m [x_m - a \cos 2\pi f(t_m - \tau) - b \sin 2\pi f(t_m - \tau)]^2 \tag{A7}$$

In Eq. A7, x_m is a signal with zero mean. The $E(a, b)$ will be minimum if both derivatives $\partial E(a, b)/\partial a$ and$\partial E(a, b)/\partial b$ are equal to zero. Adopting the notation

$$\begin{aligned}
CC &= \sum_m \cos^2 2\pi f(t_m - \tau) \\
SS &= \sum_m \sin^2 2\pi f(t_m - \tau) \\
CS &= \sum_m \cos 2\pi f(t_m - \tau) \sin 2\pi f(t_m - \tau) \\
XC &= \sum_m x_m \cos 2\pi f(t_m - \tau) \\
XS &= \sum_m x_m \sin 2\pi f(t_m - \tau)
\end{aligned} \tag{A8}$$

we are led to solve the normal equations

$$\begin{bmatrix} CC & CS \\ CS & SS \end{bmatrix} \begin{bmatrix} a \\ b \end{bmatrix} = \begin{bmatrix} XC \\ XS \end{bmatrix} \tag{A9}$$

After solving Eq. A9 to minimize E, we obtain the following expressions for the parameters a and b

$$a = \frac{XCSS - XSCS}{SSCC - CS^2} \qquad b = \frac{XSCC - CSXC}{SSCC - CS^2} \tag{A10}$$

Lomb (1976) selected the arbitrary delay τ, to simplify the normal equations (Eq. A9), by assuming that

$$CS = \sum_m \cos 2\pi f(t_m - \tau)\sin 2\pi f(t_m - \tau) = 0 \quad \text{(A11)}$$

The condition given by Eq. A11 yields a simple expression for τ in terms of f and t_m

$$\tan(4\pi f\tau) = \frac{\sum_{m=1}^{M} \sin 4\pi f t_m}{\sum_{m=1}^{M} \cos 4\pi f t_m} \quad \text{(A12)}$$

Using Eq. A11 the expressions for the parameters a and b are simplified, completing the calculation of x_f

$$a = \frac{XC}{CC} \qquad b = \frac{XS}{SS} \quad \text{(A13)}$$

By definition the power in the harmonic component of frequency f is given by $P = \sum_m x_m x_m^*$, where x_m^* is the complex conjugate. In the case of a real signal the power simply becomes

$$P = \frac{1}{2} \sum_m x_m^2 \quad \text{(A14)}$$

The factor of 1/2 is introduced to account for the fact that power is equally distributed between positive and negative frequencies. By substituting Eq. A7 into Eq. A14 we obtain the expression for the least-square spectrum

$$P = \frac{1}{2} \sum_m x_m^2 = \frac{a^2}{2} CC + \frac{b^2}{2} SS \quad \text{(A15)}$$

Substituting the parameters a and b (Eq. A13) into Eq. A15 we derive the theoretical power of the signal based on the model proposed by Lomb

$$P = \frac{1}{2}\left(\frac{XC^2}{CC} + \frac{XS^2}{SS}\right) \quad \text{(A16)}$$

Finally, expanding Eq. A16, the Lomb normalized periodogram as a function of frequency is defined by

$$P_M(f) \equiv \frac{1}{2\sigma^2}\left\langle \frac{\{\sum_{m=1}^{M} x(t_m)\cos[2\pi f(t_m - \tau]\}^2}{\sum_{m=1}^{M} \cos^2 2\pi f(t_m - \tau)} + \frac{\{\sum_{m=1}^{M} x(t_m)\sin[2\pi f(t_m - \tau)]\}^2}{\sum_{m=1}^{M} \sin^2 2\pi f(t_m - \tau)} \right\rangle \quad \text{(A17)}$$

The delay τ is a kind of offset that makes $P(f)$ completely independent of shifting all the t_i values by any constant. Adopting the definition for τ with Eq. A12 preserves the simple statistical behavior such as time translation invariance of Eq. A17, which is identical to that for an even sampling. Scargle (1982) shows that Eq. A17 can be reduced to the classical periodogram if the sampling is even, or if $\tau = 0$. Equation A17 is identical to the equation obtained if one estimated the harmonic content of a data set at a given angular frequency f, by linear least-squares fitting (Scargle, 1982). Note again that τ, a, and b are calculated once for each frequency.

The power calculated from the Lomb model (Eq. A17) is normalized by the variance

$$\sigma^2 = \frac{1}{M-1} \sum_m (x_m - \bar{x}_m)^2 \quad \text{(A18)}$$

This normalization makes $P_M(f)$ exponentially distributed with unit mean. Therefore the probability that $P_M(f)$ will be between some positive values z and $z + dz$ is exponential and depends on the number of natural frequencies M. The false-alarm probability (Press et al., 1989) $P(<z) \equiv 1 - (1 - e^{-z})^M$, gives the probability that any of the calculated frequencies will exceed the critical value z. This provides a statistical significance test for every frequency peak, making it possible to distinguish real periodicities from noise.

The time delay (τ, Eq. A12) and the statistical significance test above make the Lomb method absolutely free from aliasing. It can find spectral peaks at frequencies that are as much as 50 times higher than the Nyquist frequency based on the mean sampling frequency ($1/2\Delta$). Horne and Baliunas (1986) estimated that the number of linearly independent frequencies calculated needs to be at least equal to the number of points in the time series. For all calculations the number of frequencies M_f was selected to be twice the number of points in the time series. This ensures a better resolution of the frequency peaks in the spectrum. The smallest frequency is calculated based on the total time (T_{tot}) period and the highest one is calculated based on the Nyquist criteria determined for the mean sampling interval. Data that are closely clumped are not truly independent and will reduce the number of frequencies that can be independently determined. The integral of the estimated spectrum depends strongly on the highest frequency for which the estimate is calculated. The maximum frequency has no upper limit, so the least-square spectrum estimate, defined by Eq. A17, has no direct interpretation as a distribution of power over the frequencies. The Lomb algorithm requires $M \log_{10} M_f$ operations to calculate M_f frequencies from M data points. A C++ algorithm implementing the Lomb method is given by Press et al. (1989).

Manuscript received Oct. 9, 2003, and revision received Apr. 12, 2004.